

Graph–Property Relationships for Complex Chiral Nanodendrimers

Vera Kuznetsova,[▼] Alain Kadar,[▼] Anita Gaenko, Engin Er, Tao Ma, Kody G. Whisnant, Jessica Ma, Bing Ni, Natasha Mehta, Ji-Young Kim, Yurii K. Gun'ko, and Nicholas A. Kotov*



Cite This: *ACS Nano* 2025, 19, 6095–6106



Read Online

ACCESS |

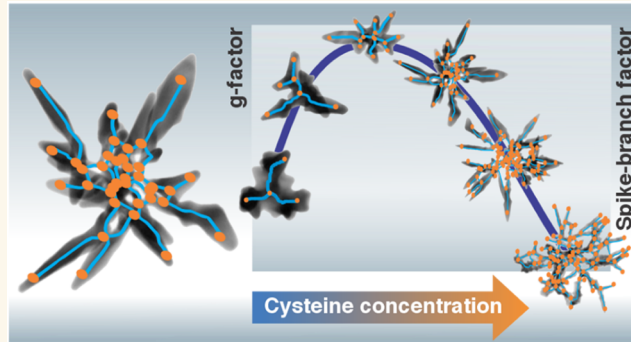
Metrics & More

Article Recommendations

Supporting Information

ABSTRACT: Organic, polymeric, and inorganic nanomaterials with radially diverging dendritic segments are known for their optical, physical, chemical, and biological properties inaccessible for traditional spheroidal particles. However, a methodology to quantitatively link their complex architecture to measurable properties is difficult due to the characteristically large degree of disorder, which is essential for observed property sets. Here, we address this conceptual problem using dendrimer-shaped gold particles with distinct stochastic branching and intense chiroptical activity using graph theory (GT). Unlike typical molecular or nanostructured dendrites, gold nanodendrimers are two-dimensional, with branches radially spreading within one plane. They are also chiral, with mirror asymmetry propagating through multiple scales. We demonstrate that their complex architecture is quantitatively described by image-informed GT models accounting for both regular and disordered structural components of the nanodendrimers. Furthermore, descriptors integrating topological and geometrical characteristics of particle graphs provide physics-based analytical relations to the nontrivial dependence of optical asymmetry *g*-factor on the particle structure. The simplicity of the GT models capable of capturing the complexity of the particle organization and related light–matter interactions enables the rapid design of scalable nanostructures with multiple functions.

KEYWORDS: chiral nanostructures, fractals, complexity, nonrandomness, biomimetics, self-assembly, graph algorithms



INTRODUCTION

Nanoscale colloids with dendritic, spiky, and networked architectures enable multiple applications because of their dispersion stability, surface area, photonic activity, and biological functions. Their structures can display deterministic bifurcation sequences with varying degrees of regularity and stochasticity. Examples include spheroids from poly(amidoamine), poly(phenyl acetylene), and similar bifurcating subunits emanating from the same atomic center, known as dendrimers.^{1–4} They belong to a large family of complex particles with radial symmetry that also include polymer-grafted nanoparticles (NPs),⁵ “hairy” polymers,⁶ branched polymeric particles,⁷ and inorganic supraparticles.⁸

While dendrimers display radial symmetry, the regularities in the architecture of other particles in this family can be obscure. One such group is the particles where the branching segments are 10–100 nm in length, which can be described as nanodendrimers. Their spatial organization is more stochastic⁹ than molecular dendrimers because the nanodendrimers are typically self-assembled from NPs that are polydisperse. When nanodendrimers display radial geometry, their branching

segments are referred to as spikes, rays, or petals.^{9,10} Fittingly, the particles composed of such segments are referred to as nanoflower-,¹⁰ hedgehog-,^{11,12} star-,^{13–15} snowflake-,¹⁶ or urchin-like^{17,18} particles or colloids. Similar radially diverging segments form a stratum of spikes around particles with cylindrical symmetry that are referred to as centipede-like.¹⁹

As observed empirically, the physicochemical properties of all of these particles are dependent on size, connectivity patterns, and branching sequences. However, extracting quantitative dependences even from systematic empirical data for nanodendrimers is fundamentally hard. This is because the known approaches to describe the chemical structure of classical crystals, liquid crystals, quasicrystals,

Received: September 14, 2024

Revised: January 7, 2025

Accepted: January 8, 2025

Published: February 4, 2025



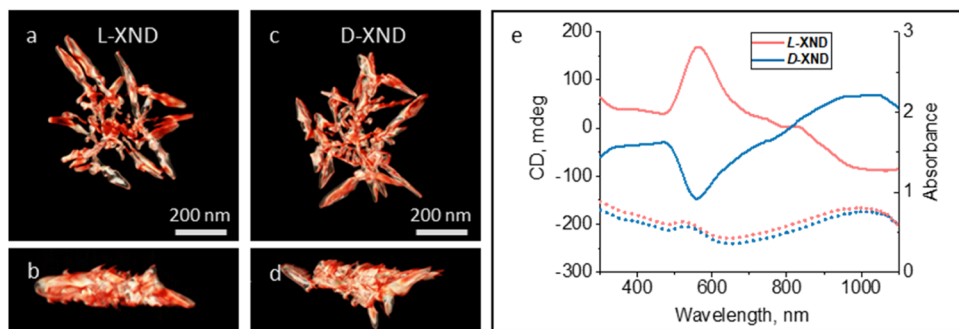


Figure 1. Transmission electron tomography of L-XND (a, b) and D-XND (c, d): top view (a, c) and side view (b, d). (e) UV-vis (dotted lines) and CD (solid lines) spectra of L-XND (red) D-XND (blue), $[Cys] = 3.6 \mu M$.

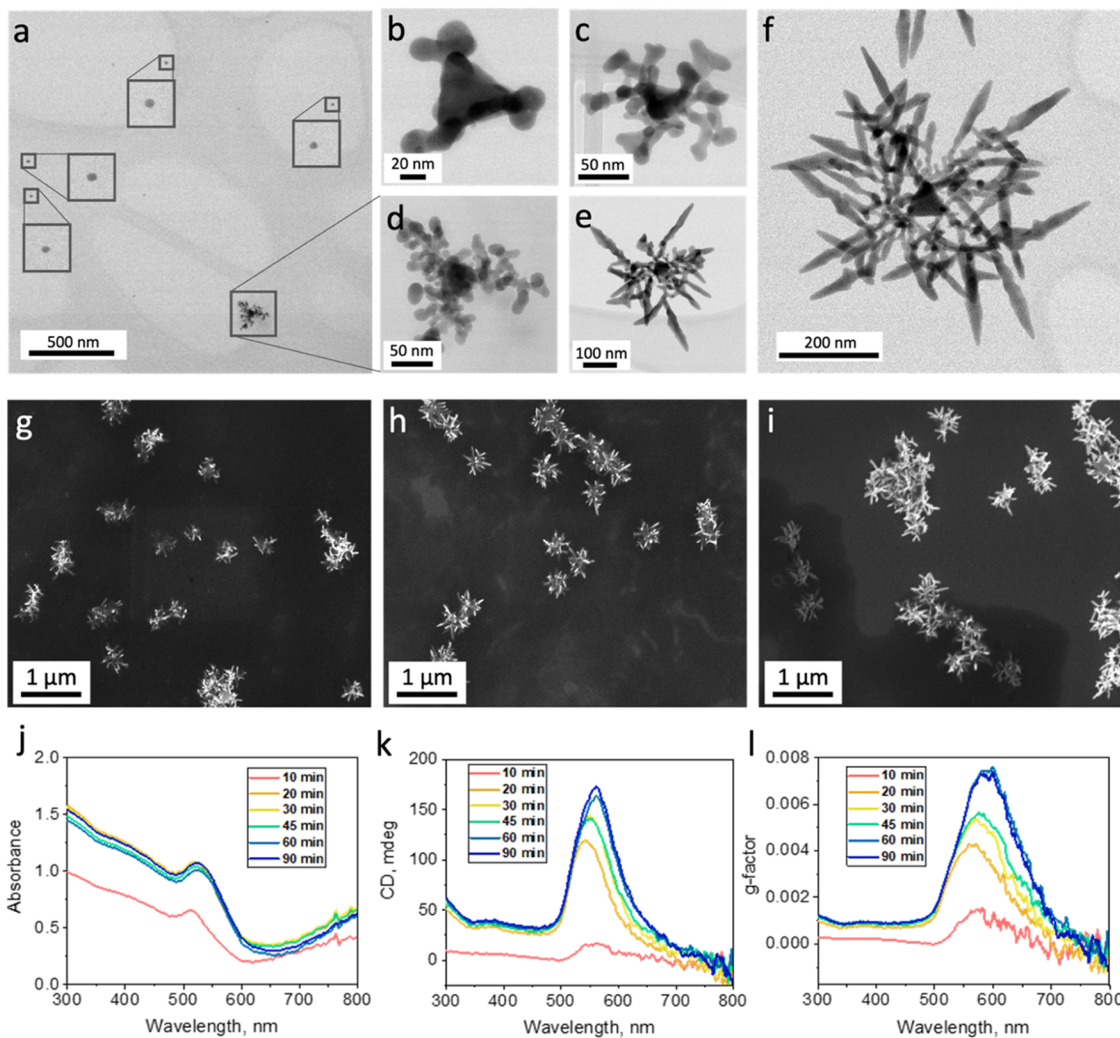


Figure 2. Electron microscopy images and optical spectra of L-XNDs at different time points of their synthesis. (a) Survey TEM image of multiple particles at $t = 3$ min. (b-f) TEM images of single particles at $t = 1, 3, 5, 10$, and 90 min. (g-i) SEM images of particles at $t = 10, 20$, and 90 min. (j) UV-vis, (k) CD, and (l) g-factor spectra for L-XND for $t = 10-90$ min with $[Cys] = 3.6 \mu M$.

polymer conformations, or glasses become inapplicable to structural patterns with a high variability and stochasticity observed in many biological, biomimetic, and bioinspired materials.

The quantitative description of nanodendritic architectures was attempted using the theory of fractals.^{20–23} However, the applicability of mathematics of fractals to the NP agglomerates is limited by the lack of multiple scales of self-similarity and

sufficient variability of the branching segments. Nanodendrites produced by agglomeration of NPs may have an appearance of fractals.²⁴ But, strictly speaking, they do not conform to Mandelbrot's mathematical framework of fractals. Consequently, the range of fractal dimensions in nanodendrites and other molecular or nanostructured materials is narrow and nonspecific.^{20–23} The recent experimental data also show that NP agglomeration patterns strongly deviate from fractal

patterns even when there is a strong influence of diffusion-controlled transport²⁵ that typically results in fractality of microscale assembled micrometer-scale colloids²⁶ or angstrom-scale molecules.²⁷ Last but not least, the fractal metrics are unitless and, so, cannot be easily mapped to material properties that typically have physical units.

We also note that the need to develop methods of structural description for molecular and nanoscale dendrimers is acute because these materials possess a unique combination of properties that is nearly impossible to obtain otherwise. For example, organic dendritic materials possess chemical,³ rheological,²⁸ adhesion,⁷ and biomedical²⁹ properties that cannot be easily obtained in linear molecules, smooth particles, or continuous crystals. Similarly, inorganic dendrites display unusual chemical,^{30,31} electrical,³² thermal,^{33,34} optical,¹⁶ and biological^{35,36} properties attributed to the stochastic organization of these materials. As evidence of their technological significance, multiple examples of branching, spiky, and networked nanomaterials can be found in energy storage, plasmonic catalysis, biomedical implants, and desalination membranes. Complex nanostructures combining order and disorder are preferred³⁷ because they enable continuously variable properties in response to gradually increasing environmental pressures. On the contrary, perfect crystalline phases are associated with discontinuities due to phase transitions. As evidenced by their abundance in Nature, materials with variable degrees of organization also afford tuning of multiple properties simultaneously, which is essential for survival of an organism adapting to rapidly changing environmental conditions. Acceptance of the necessity of stochastic imperfections in high-performance materials also makes them synthetically more accessible. Structural models needed for complex materials should (1) accurately capture their convoluted architectures and (2) be scale-agnostic because complex organizational patterns may emerge at atomic, nanometer, micrometer, and other ranges. Such a framework should enable better understanding of their multiple properties, including light scattering, charge accumulation, viscoelastic behavior, and biological activity, enabling new structure–property relations.

RESULTS AND DISCUSSION

Synthesis and Characterization of Complex Nanodendrimers. Relating the complex structure of nanodendrimers to their properties requires an experimental model system that combines (1) high-contrast imaging tools for accurate evaluation of the structure, (2) properties strongly dependent on branching patterns, and (3) synthetic control of stochastic architecture for sufficient variability and generality. Here, we synthesized gold nanodendrimers that conform to these requirements, taking advantage of the well-known seed-mediated growth catalyzed by the premade metal particles of smaller size. Specifically, we used trigonal prisms of gold with sides of 60–70 nm as seeds dispersed in solutions of HAuCl₄ in the presence of the amino acid cysteine (Cys). Ascorbic acid (AA) served as the reducing agent, while cetyltrimethylammonium chloride (CTAC) or bromide (CTAB) helped dispersibility of the produced particles as labile surface ligands. The branching spikes radiated predominantly from the vertices of the prisms and had lengths of 200–300 nm (Figure 1a,c).

The particle morphology was evaluated for different durations of the synthesis, *t*. TEM images of single particles indicate that the dendritic morphology is acquired via gradual

growth/assembly from the common center (i.e., seed particle), which is analogous to the polymerization process (Figure 2a–f),³⁸ which was also confirmed by SEM (Figure 2g–i). The maximum amplitudes of UV–vis and related spectra tend to increase for 10 min < *t* < 60 min and then plateau for *t* up to 90 min (Figure 2j–l). The maxima in all spectra shift to the red due to the interspike plasmonic coupling with increasing particle size and branching.

The structure of the synthesized nanodendrimers is controlled by Cys concentration, i.e., [Cys]. When [Cys] = 0, NPs with polyhedron shapes are formed (Figure S1).^{33,39–43} As [Cys] rises from 0.125 to 36.2 μM, while maintaining [HAuCl₄] = 0.37 mM, the size of the nanodendrimers, the length of the spikes, and the generation number increase. When the Cys surface ligands were enantiopure, the spikes became twisted. The peaks in CD and g-factor spectra indicate the chirality of the particles (also see the Graph Models of XND section).

Overall, these particles can be referred to as complex chiral nanodendrimers and abbreviated as XNDs, where X stands for both complex and chiral. Note that they are unique among nanostructures and among dendrimers. Unlike polyamidoamine (PAMAM) and similar polymeric dendrimers with a deterministic bifurcation sequence, XNDs are large and stochastic. While one can identify the 0th, 1st, 2nd, 3rd, 4th, etc. levels of bifurcation in TEM images, the branching generation is nondescriptive of XNDs structure due to variable lengths of the linear segments. Unlike polymer brushes, spherical amino acids, “hairy” polymers, microparticle fractals, etc., the linear segments in XNDs are nanoscale in length and thickness. This change in geometry also makes them rigid, which is essential to their colloidal behavior and simplifies modeling. Unlike other particles with spiky morphologies, XNDs are predominantly two-dimensional (2D) because the branching segments grow preferentially within the same plane as the original prism (Figure 1a–d). The “flatness” of the spiky particles is attributed to the tendency of reaction intermediates, i.e., small gold NPs to attach in epitaxial manner to each other.⁴⁴ Also, strong electrostatic repulsion of the NPs from the central part of the prism (due to the highly charged layer of cetyltrimethylammonium cations) makes out-of-plane localization of NPs energetically less favorable than the peripheral attachment to the growing linear segments.

Multiscale Chirality of XNDs. Unlike most dendritic structures, these particles are mirror asymmetric as indicated by their strongly enhanced chiroptical activity (sometimes referred to as “giant”) exceeding that of Cys by at least 50 times (Figures 1e and 2k,l). The geometric property of chirality is worth special consideration here because XNDs display chirality at multiple scales, which is directly related to their structural complexity. One level of chirality is at the scale of ~3 Å; it is characteristic of the α-carbon atom in Cys attached to the surface of gold, which is responsible for the appearance of the peak in the CD and g-factor spectra at ~260 nm (Figure 2k,l).

The next level of chirality is at a scale of ~50 nm characteristic of the pitch of the helical spikes. L-Cys promoted the formation of the right-handed spikes; when D-Cys is used, the left-handed spikes dominate. The nanoscale chirality is responsible for the CD peaks at ~530 and ~1030 nm, corresponding to transverse and longitudinal plasmonic modes propagating in the nanoscale spikes, respectively. The nanodendrimers made with L-Cys (i.e., L-XNDs) displayed a

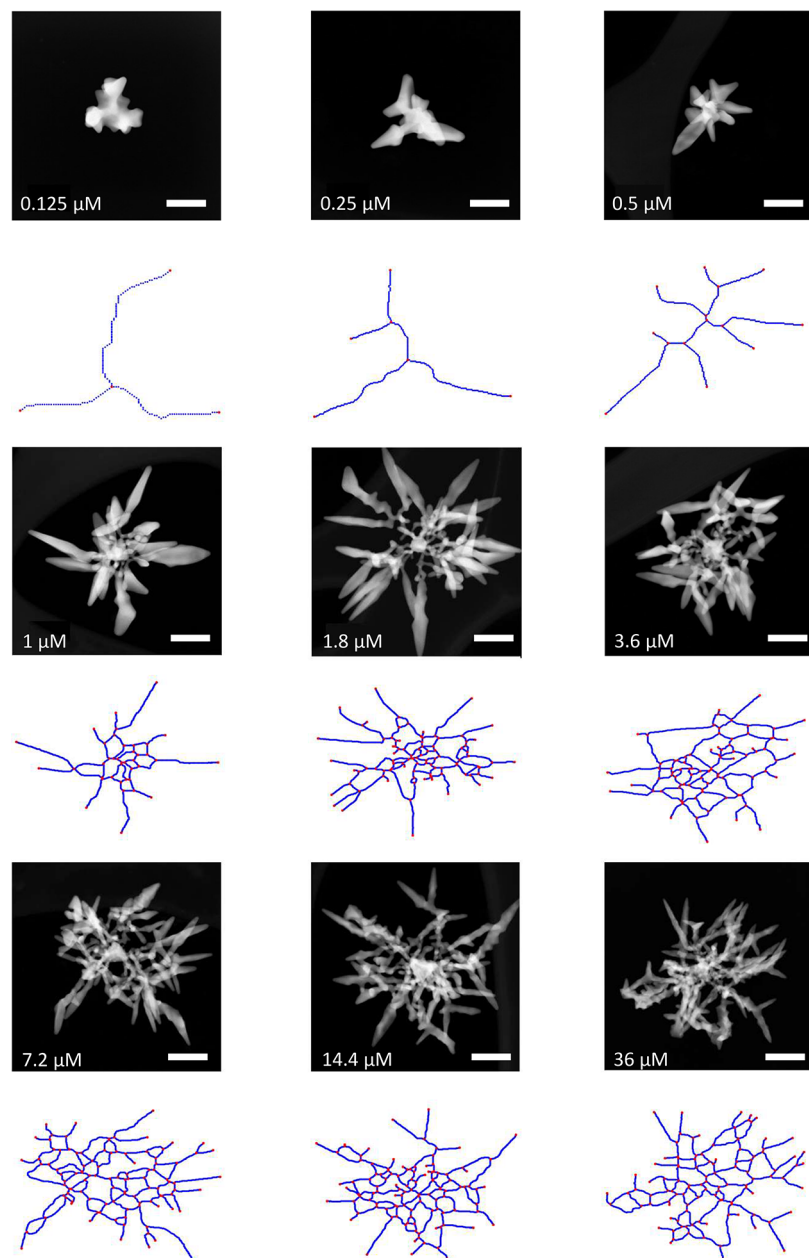


Figure 3. TEM images and corresponding graph representations of XNDs of various sizes and branch generations for $0.125 < [\text{Cys}] < 32.2 \mu\text{M}$. Scale bar in all images is 100 nm; the graph models below the TEM images were acquired with *StructuralGT*.⁵⁰

positive transversal and negative longitudinal circular CD peaks, with the opposite handedness for XNDs made with d-Cys (i.e., d-XNDs, Figure 1e). The peaks are strongly broadened compared to gold nanorods due to the spike-to-spike plasmon coupling and stochastic organization of the nanodendrites. The amplitude of the g-factors consistently increased with the reaction time, which indicates the increase of mirror asymmetry at nanometer scale responsible for the 530 nm plasmonic peaks.

Besides the angstrom and nanometer scales of chirality, the overall geometry of the XNDs at 100–500 nm scale (often referred to as mesoscale, i.e., intermediate between nano and micro scales), can also be chiral and may have a consistent preference toward left- or right-handed shapes. However, the CD spectra of the XNDs alone are insufficient for the assessment of the mesoscale chirality due to similarity of their

optical manifestation to nanoscale. To understand the contribution to the mesoscale chirality of XNDs to their optical properties, they were etched using the 6 μM HAuCl₄ solution for 2 h.⁴⁵ As expected, the branched XND architecture was gradually destroyed (Figure S2a,c) and the chiroptical activity concomitantly diminished (Figure S2d). Nonetheless, the g-factor spectra of the etched XNDs retained a weak but distinct positive peak at 550 nm (Figure S2d) descriptive of the mirror asymmetry of the central section of XNDs. Combined with the UV-vis extinction spectra (Figure S2e), these data indicate that the 3D arrangement of spikes is chiral, corresponding to the third level of chirality at 200–300 nm scale.

To gain an additional proof of the necessity of mesoscale chirality for the optical properties, we also grew a gold overcoat in an achiral growth media on top of the L-XNDs,⁴⁶ which

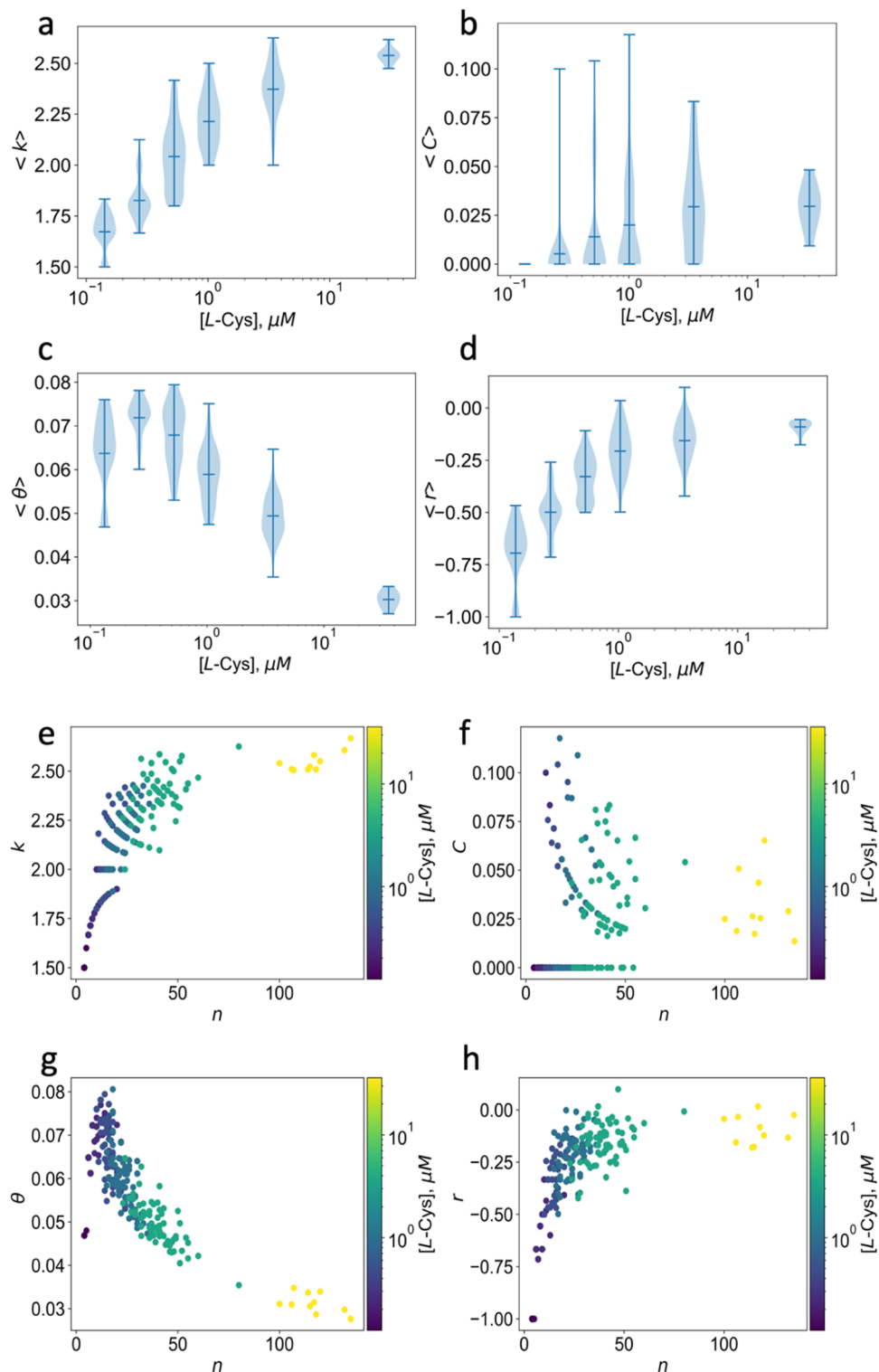


Figure 4. Dependences of GT parameters, namely, average degree ($\langle k \rangle$), clustering coefficient ($\langle C \rangle$), assortativity coefficient ($\langle r \rangle$), and betweenness centrality ($\langle \theta \rangle$) on L-Cys concentration, i.e., [L-Cys] in violin plots in (a-d), and the number of nodes, n , in (e-h).

results in smooth untwisted spikes (Figure S3a,b). If the optical activity in the plasmonic region came only from the twist of the spikes, then these particles should reveal strongly diminished optical activity (Figure S3b). However, the g-factor plots showed a red shift, while the broad peak in the extinction spectrum centered at ~ 530 nm merged with the long tail (Figure S3e,f). Eventually at a higher ratio of HAuCl₄ to XND seeds, the gaps between the linear segments become filled and

the particles lose their dendritic morphology (Figure S3c,d). Still, a portion of optical activity remained, which confirmed the existence of chirality at the mesoscale. We confirm this point by calculation of chirality indices from tomography data (Osipov–Pickup–Dunmur and Hausdorff Chirality Measure; details in the Supporting Information). Considering that the circular dichroism of dispersions is determined by 3D chirality,

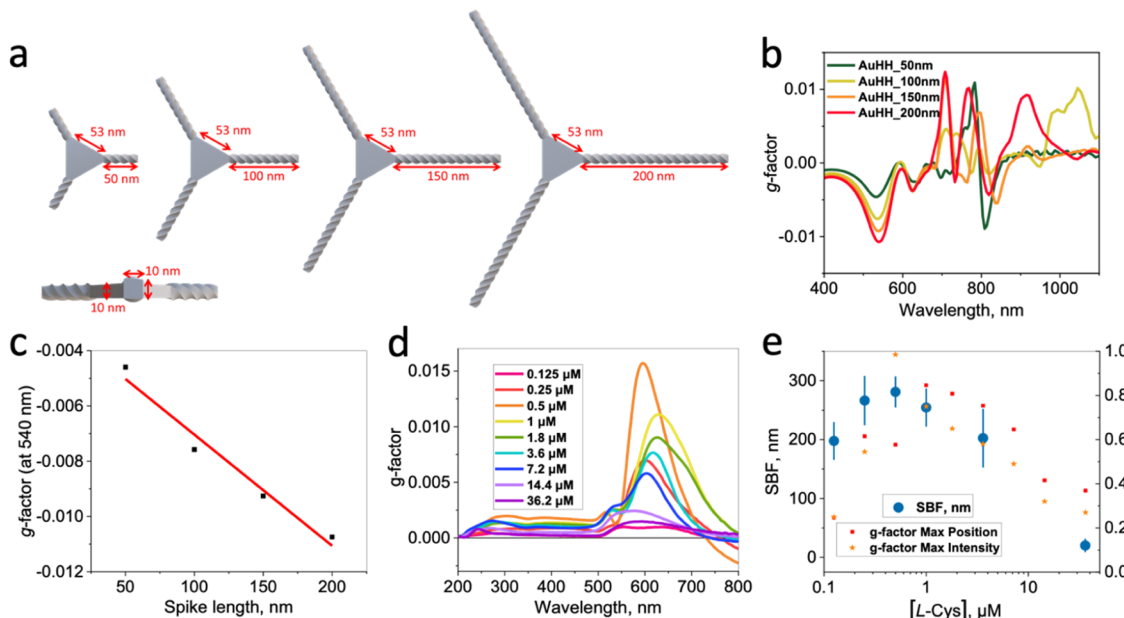


Figure 5. Electromagnetic simulations of idealized bifurcating segments in idealized XNDs. (a) Dimensions of simulated structures. (b) Simulated g-factor as a function of wavelength and spike length. (c) Linear fitting between transverse spike mode g-factor and spike length. (d) Experimental g-factor data for XNDs at different concentrations. (e) Graph–property relationship between [L-Cys], (SBF), and g-factor.

the overall dimensionality of XNDs becomes intermediate between 2D and 3D.

Graph Models of XND. Chiroptical activity in the visible range is dependent on geometrical (e.g., diameter of particle, length of segments) and topological (e.g., number of spikes, frequency of bifurcations) characteristics of XNDs. Furthermore, all of these have large statistical variations. Conventional electromagnetic models of plasmonic particles might be possible for some of the XND segments, but statistical variations of multiple parameters make these simulations prohibitively expensive. Interdependence of different structural parameters reflecting the combination of order and disorder in XNDs can be accounted for by GT. The dendritic architecture can be represented as a graph, $G = (N, E)$, or a set of nodes, N , interconnected by edges, E , which can be derived from electron microscopy images. The nodes represent the bifurcation points at which new branches are formed, while the edges represent the linear segments between them. Compared with the theory of fractals, GT offers a much larger number of structure descriptors. Furthermore, GT descriptors do not impose any rigid framework on structural motifs and are scale-agnostic.

Graph models have been successfully used in the past for the phenotyping of plants⁴⁷ and analysis of convoluted architectures of self-assembled nanoscale assemblies represented by hedgehog particles from AuS nanosheets⁴⁸ and percolated network materials of aramid nanofibers.⁴⁹ Compared to them, the “flatness” of XNDs makes them particularly suitable for establishing analytical graph–property relations because the GT parameters extracted from 2D projections in traditional microscopy images are exact replicas of the original particles (Figure 1). The graphs of XNDs can also account for the effect of the structural variability (Figure 3) on the optical effects.

Using TEM images and the computational package *StructuralGT*,⁵⁰ we calculated the ensemble-averaged GT parameters for graph models of XNDs, denoted as $\langle \bullet \rangle$. Simple parameters such as number of nodes and edges ($\langle n \rangle$ and $\langle e \rangle$)

can serve as GT proxies for average particle sizes. Additional GT descriptors include nodal degree, k , i.e., the number of edges connected to a node, and clustering coefficient, C , i.e., the measure of the number of triangles in a graph. We also calculated the assortativity coefficient, r , that reflects the correlation of k between pairs of linked nodes. When $r > 0$, the adjacent nodes tend to have a similar degree; when $r < 0$, the linked nodes tend to have different degrees; $r = 0$ implies that a node's k and the k of its neighbors share no correlation. We also calculated betweenness centrality, θ , that is, the ratio of the shortest paths passing through the specific node, to the total number of the shortest paths connecting the nodes in the set. This quantity characterizes the importance of each node in providing long-range connectivity across the entire XND. k and C characterize the short-range organizational pattern, and r and θ characterize the medium- and long-range organizational patterns, respectively. Direct quantification of the complexity of synthesized structures can also be attained using other GT tools, such as chromatic numbers.⁴⁶ To provide a better understanding of how k , C , and θ vary within a single XND, we overlay their value at each node for a series of XND TEMs in Figure S4. We also give examples of model graphs with high and low r values in Figure S5.

Confirming the visual observations from TEM, the dependence of $\langle k \rangle$ on [L-Cys] (Figure 4a) indicates a gradual increase of branching. The emergence of the peak for $\langle C \rangle$ at low [L-Cys] indicates the onset of the formation of the complex structures represented by the emergence of edges interconnected into triangles (Figure 4b). The gradual decrease of $\langle C \rangle$ and $\langle \theta \rangle$ when [L-Cys] > 0.125 μM/L reflects the self-limited growth of the particles (Figure 4c,d) and corresponds to the formation of the spikes, i.e., peripheral and terminal edges. From the GT perspective, the spikes are the edges that have nodes with $k = 1$. Hence, their connectivity is lower than the edges in the central part of XNDs, which results in the decrease of particle-average values of C and θ , as the number of spikes increases (Figure 4c,d).

The conversion of the dependence on $[L\text{-Cys}]$ (Figure 4a–d) into dependence on n (Figure 4e–h) shows the effects specific to discrete mathematics as exemplified by “banding” of experimental points for $\langle k \rangle$ and $\langle C \rangle$ when $n < 50$ (see details in the Supporting Information). Of note, the dependence of $\langle C \rangle$ vs n (Figure 4f) is split into a zero and nonzero cluster of points, which originates from the fact that C considers cycles of only three nodes, whose average number is affected both by the emergence of less connected spikes at $n \sim 50$ and the gradual increase of branching generations $n > 50$. The rapid decrease of assortativity coefficient r approaching zero for high n indicates the increase of the short-range disorder in XND organization as the particle size increases. Concomitantly, narrow variations of $\langle k \rangle$ quantitatively reflect the short-range order of their structural patterns.

Considering GT-based property relationships, we note that “banding” of k and C (Figure 4e,f) makes them unfavorable candidates compared to θ and r for this specific nanoscale material (Figure 4g,h). Importantly, the similarity of trends observed for $\langle \theta \rangle$ and, for instance, g-factor (Figures 4c and 5a) are coincidental rather than causative (see details in the Supporting Information). Nevertheless, the n -dependences of k , C , r , and θ lead to important insight. The number of nodes in large XNDs is ~ 100 , which is small by the standards of network science. Nevertheless, it is sufficient to observe the asymptotic behavior of $\langle \theta \rangle$, $\langle k \rangle$, and $\langle r \rangle$, which indicates that the complex structural patterns of nanoscale structures can indeed be realistically captured by the GT parameters.

Graph–Property Relationship for Chiroptical Activity. The chiroptical activity of XNDs offers an important test case for establishing graph–property relationships because (1) multiple structural parameters relevant to light–matter interactions are captured by the GT models: i.e., linear segments, junctions, spikes, etc., and (2) none of these structural features dominate the plasmonic properties, leading to extremely convoluted structure–polarization dependences and nonlinear trends, which makes graph models particularly convenient. Furthermore, multiple scales of chirality found in XNDs affect the chiroptical spectra. Thus, the structural patterns at multiple scales responsible for mirror asymmetry should be accounted for.

Some monotonic and linear relationships, exemplified by the gradual increase of peak intensity and red shift in Figure 2j–l are relatively obvious and do not need GT. While they could be represented as the dependence on n , they can be much better rationalized based on XND size. The dependence of g-factor at 540–560 nm obtained for different $[L\text{-Cys}]$ showed, however, an unexpected nonlinear and nonmonotonic behavior with distinct maximum for particles at intermediate $[L\text{-Cys}]$ (Figure 5a). Chiroptical properties are a very different case from past applications of GT related to mechanical, thermal, and electrical properties,^{51–54} where the graphs and networks make GT application intuitive. The utility of those nanomaterials is predicated on the account of transport phenomena that are natural for the graph models. In the case of optical properties, what comes into focus is the ability of GT to account for both order and disorder.

Being informed by the optics of plasmonic nanostructures,^{55–58} one can expect that the spikes would have a larger contribution to plasmonic activity than segments inside the nanodendrimers.^{59,60} Because we know that the g-factor at 540 nm corresponds to the transverse plasmonic mode, we expect it should increase with spike length. The presence of

neighboring spikes and their collective stochasticity strongly influence the polarization rotation and thus need to be accounted for explicitly. To make a step toward such structure–property dependence, we carried out simple finite-difference time-domain (FDTD) simulations of idealized structures to confirm the importance of spikes in the optical activity of XNDs overall (Figures 5b and S6–S11, see the Methods section). We found that the g-factor at 540 nm correspondingly to the transverse plasmonic mode linearly increased with the length of idealized spikes (Figure 5c,d). By other words, one can expect that for complex and nonideal structures g-factor is proportional to S , where S is the sum of spike lengths of a single particle in nanometers. To transition from idealized structures that can be modeled to realistic structures that are highly variable, we hypothesize that the reduction in g-factor at higher $[L\text{-Cys}]$ is caused by the presence of highly connected nodes that induce plasmonic coupling around spikes. This hypothesis is confirmed by the similar coupling effects that have been shown to reduce plasmonic activity in NP aggregates in the exponential fashion, $f = \exp(\text{distance between NPs})$.⁶¹ It naturally extends to the chiroptical spectra. For example, as proximity increases, the chiral component of the optical spectra (i.e., arising from the enantiopure twist) will tend to 0, and so will the g-factor. Thus, we calculated the number of branch points, B , as the total difference between k and 2 for a single XND (e.g., a node with 3 edges emanating from it implies $B = 1$; A node with 10 edges emanating from it implies $B = 8$). Considering that g-factor should linearly increase with S and exponentially decrease with B ,⁶¹ we define the spike-branch factor, SBF as $\text{SBF} = S \exp(-\beta B) \sim g\text{-factor}$, where β is a preexponent. For clarity of the mathematical approach and procedures, we show how S , B , and SBF are calculated for a series of model structures in Figure S12. Figure S14 displays how S and B change with $[L\text{-Cys}]$. Taking β as a fitting parameter, an analytical expression correlating SBF and the g-factor can be found (Figure 5e) using the data from Figure 3 as inputs. In Figure S15, we show how SBF changes with n . The decrease in both SBF and g-factor for $[Cys] > 1 \mu\text{M}$, suggests that connectivity patterns are the dominant source of variation in nanoscale chiroptical activity for XNDs, captured by B .

Graph Hamiltonians for XNDs. While the above findings offer a foundational first step in the development of graph–property relationships for complex nanostructures, caution should be taken when extending this work to new systems, especially when geometry plays a large role. Although GT description of highly symmetric systems (e.g., colloidal crystal) is possible, enthusiasm for its use should be combined with assessment of its necessity. For example, detection of phase transitions and bandgaps in crystalline structures is made possible by Steinhardt order parameters⁶² (among others) and Bloch’s theorem,⁶³ respectively. It is only when we seek to detect, however, the same phenomena in complex structures (i.e., those that combine order and disorder) that methods of StructuralGT parameters⁶⁴ and quantum graphs⁶⁵ offer their greatest utility. Such studies will be enhanced further by leveraging tools from probability theory (see the Supporting Information for an example of artificial XND generation).

It is also relevant to note that simulations of colloidal crystallization have been carried out in conventional position-momentum phase space for a vast array of particle shapes and interactions.^{66–68} While transitioning to a GT approach for the study of such crystallizations offers a level of coarse-graining

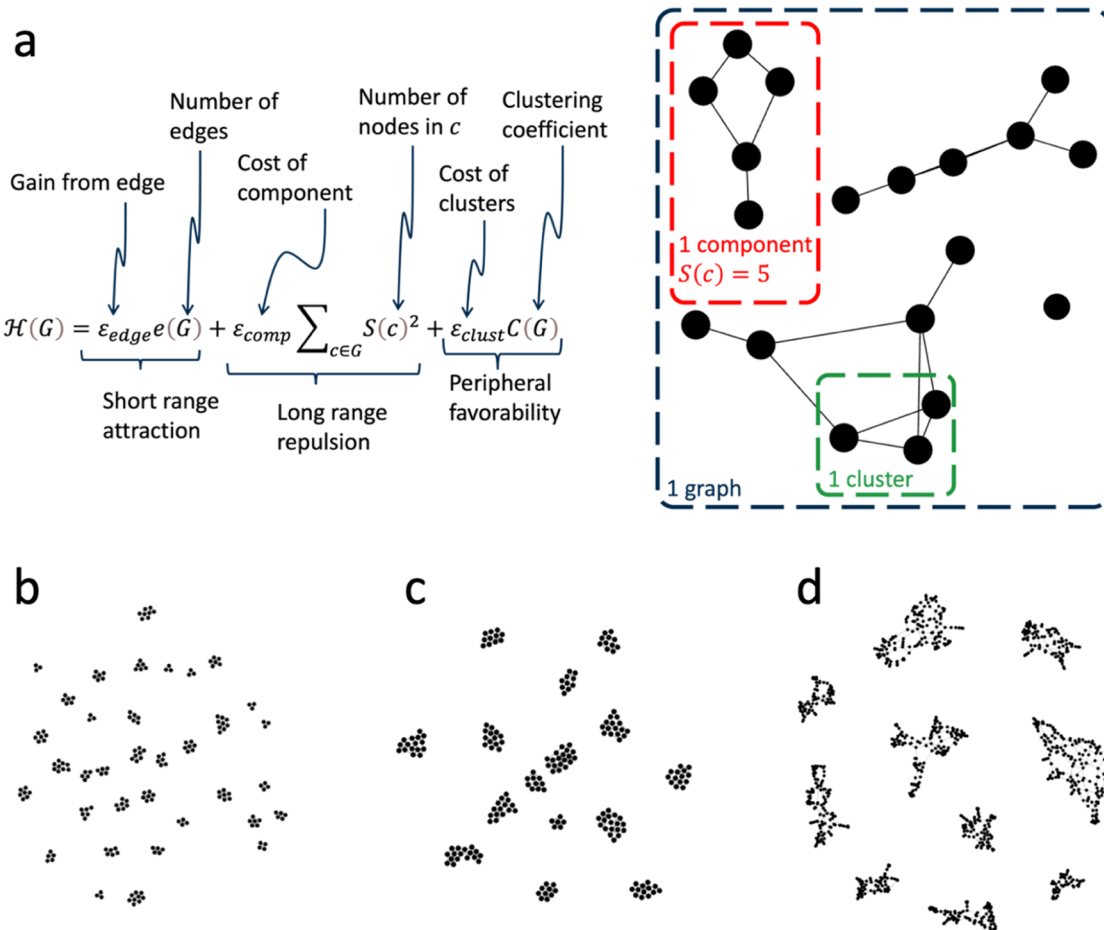


Figure 6. Graph Hamiltonian methods for computational XND analysis and generation. (a) Schematics of the graph Hamiltonian with labels for each of the terms, and a schematic to give examples of corresponding graph structural motifs. (b–d) Examples of graphs governed by the Hamiltonian representing XND made under different conditions described by different values of $\varepsilon = (\varepsilon_{\text{edge}}, \varepsilon_{\text{comp}}, \varepsilon_{\text{clust}})$: (b) $\varepsilon = (-1.5, 3, 0)$; (c) $\varepsilon = (-5, 3, 0)$; (d) $\varepsilon = (-5, 3, 10)$.

for the study of ever larger systems,⁶⁹ we believe it is especially powerful in its ability to efficiently circumvent the notorious problem of nonadditivity of NP interactions,⁷⁰ thus enabling simulation of complex structures, such as XNDs. To this end, we simulate their formation using a method of network Hamiltonian described by Butts et al. for the formation of disordered protein aggregates.⁷¹ In brief, the structure of a complex nanoscale system produced by self-assembling NPs can be described by a graph interconnecting them. The energy of this system is given by its Hamiltonian. Finding a specific configuration of the system corresponding to the energy minimum is carried out using a Metropolis-Hastings algorithm to add/remove edges (a discussion on the algorithm's detailed balance and ergodicity is given in the Supporting Information).⁷² Overall, the graph Hamiltonian can be expressed as

$$\mathcal{H}(G) = \varepsilon_{\text{edge}} e(G) + \varepsilon_{\text{comp}} \sum_{c \in G} S(c)^2 + \varepsilon_{\text{clust}} C(G)$$

where $\mathcal{H}(G)$ is the Hamiltonian of the graph, G ; $e(G)$ is the number of edges in G ; and $C(G)$ is the number of clusters in G . c is a component of G and $S(c)$ is the number of nodes in c . Finally, the parameters denoted as ε are the energetic costs and gains associated with each respective structural feature. Their signs and physical interpretations of the three terms are given as follows:

- $\varepsilon_{\text{edge}}$ (negative): The energetic gain associated with two particles coming into close contact with each other due to short-range attractive forces. Similar to the depth of a square-well potential used to approximate particle stickiness.⁷³
- $\varepsilon_{\text{comp}}$ (positive): The energetic cost associated with one particle joining a cluster of other particles. Included to approximate the long-range Yukawa repulsion, previously shown to be responsible for the self-limiting nature of NP assembly.⁷⁴ The quadratic form is chosen so that $\partial \mathcal{H} / \partial S(c) \sim S(c)$.
- $\varepsilon_{\text{clust}}$ (positive): The energetic cost associated with one particle forming a bond with two other particles that are already bonded (hence forming a triangle). Used to energetically favor chain-like over cluster-like morphologies. Mechanistically, this originates from the stronger electrostatic repulsion associated with a particle joining the core of a dendritic particle, as opposed to its periphery,²⁵ as well as the entropic favorability of peripheral attachment.

A more detailed discussion of how the three terms are related to classical molecular simulation is given in the Supporting Information. Figure 6a summarizes the network Hamiltonian, while Figure 6b–d give results for a few different values of ε parameters, showing that competition between

short-range attraction and long-range repulsion achieves self-limiting assembly (**Figure 6b,c**), while adding the additional term for peripheral favorability leads to dendritic morphologies (**Figure 6d**). Although this method for modeling networks is known under the name of Exponential Random Graph Models in the social sciences community,⁷⁵ its statistical mechanical formulation is a new development.⁷⁶ Its conceptual applicability to the self-assembly of nanoscale systems is advocated in this study.⁷⁷ Hence the vast array of advanced molecular simulation methods (e.g., parallel tempering,⁷⁸ cluster moves,⁷⁹ umbrella sampling⁸⁰) are simultaneously untapped and well poised to enhance the emerging field of GT for complex nanostructure design.

CONCLUSIONS

Taking advantage of synthetic control over the architecture of complex gold particles, we developed quantitative description of their dendritic structure with stochastic but nonrandom sequence of branching segments of nanoscale dimensions. Graph models accurately representing the nanoscale architecture were built based on TEM images. Analysis of GT parameters, such as the nodal degree, assortativity coefficient, clustering coefficient, and betweenness centrality, describing their short-, medium-, and long-range organizational patterns, indicates that the graph models accurately capture the complex structural patterns characteristic of XNDs. Building on these and prior findings about the structural description of complex nanostructured particles,⁸¹ composites,⁸² and biomaterials⁸³ using GT, we show the first example of analytical graph–property relations for optical properties combining the topological parameters of XNDs with geometric characteristics of spikes. Furthermore, this graph–property relation accounts for the nontrivial dependences of the *g*-factor on the gradually increasing complexity of particles. The utilization of graphs enables engineering of complex nanomaterials with simultaneous optimization of multiple functions dependent on the connectivity patterns.

METHODS AND EXPERIMENTAL SECTION

Materials. Hydrogen tetrachloroaurate trihydrate (HAuCl₄·3H₂O), cetyltrimethylammonium bromide (CTAB, ≥99%), cetyltrimethylammonium chloride (CTAC, 25 wt % in water), potassium iodide (KI, ≥99%), sodium hydroxide, (NaOH, ≥98.0%), D-cysteine (D-cys, 99%), L-cysteine (L-cys, 98%), and L-ascorbic acid (AA, ≥99.9%) were obtained from Sigma-Aldrich (Milwaukee, WI). Milli-Q water was used to prepare solutions unless otherwise stated. Ultrathin carbon film on lacey carbon support film, 400 mesh, and copper (Prod no. 01824) were purchased from Ted Pella (Redding, CA).

Synthesis of the Gold Nanoprism Seeds. This is the first step in the dendrimer preparation, based on the methods published previously.^{36,84} A 211.8 μL aliquot of CTAC solution, 25% by weight, was added to 9,338 mL of deionized water. 75 μL of 10 mM KI was stirred into the solution. In a separate small container, 80 μL of 25.4 mM HAuCl₄ was mixed with 20.3 μL of 0.1 M NaOH. This mixture was injected into the KI-CTAC solution, turning the clear solution yellow-orange. 80 μL of 64 mM ascorbic acid and the solution was quickly mixed. Then, 10 μL of 0.1 M NaOH was immediately added to the solution, and the mixture was slightly shaken. The intensity of the shaking is a key factor in the synthesis. With intensive mixing, round particles are obtained instead of nanoprisms. After 10–15 min, the solution became dark blue; a red or purple solution would indicate the formation of undesired small, round NPs. After the particles formed, they were centrifuged at 10,000 rpm for 5 min. The supernatant was drained and replaced with

approximately 1.5 mL of 5 mM CTAC. This washing procedure was repeated two more times. Once the seeds are washed, they remain stable for as long as several months if kept in the dark at 4 °C.

Synthesis of the Gold Nanodendrimers. The seeds were first diluted with 5 mM CTAC from 1.5 to around 4 mL. This stock of seeds can be used for several subsequent syntheses of dendrimers. 1.6 mL of 0.01 M CTAB solution was added to 7.9 mL of deionized water. Then, 400 μL of 10 mM HAuCl₄ was stirred in and the solution was allowed to rest for 10 min, during which it turned from pale yellow to orange. All of the solutions used for the procedures described above were made in deionized water. In rapid succession, stirring between each step, 950 μL of 40 mM ascorbic acid, necessary volume of 4 mM L- or D-cysteine (for example, to obtain the final Cys concentration 3.6 μM, 10 μL of Cys was used), and 200 μL of the previously synthesized seeds were added to the solution. The solution was left for 90 min (without stirring) before centrifuging at 10,000 rpm for 5 min, after which the dendrimers were resuspended in 1 mM CTAB or 5 mM CTAC wash solution.

Particle Etching Experiment. The protocol was adopted from the literature.⁴⁵ In a typical etching experiment, 0.5 mL of CTAB solution (10 mM) was added into 0.5 mL of Milli-Q water, and then 2 μL of HAuCl₄ solution (3 mM) was injected. The solution was sonicated for around 30 s. After that, 50 μL of a gold dendritic particle solution (the Au⁰ concentration was around 4.5 mM) was subsequently added. The solution was kept undisturbed for 2 h at room temperature. Then, the solution was centrifuged and washed with Milli-Q water.

Particle Overgrowth Experiment. The protocol of growing additional layer of gold on premade particles was adopted from ref⁴⁶. Specifically, 8 μL of HAuCl₄ solution (50 mM) was injected into 1.8 mL of hexadecylpyridinium chloride solution (0.1 M). Then, 140 μL of AA solution (0.1 M) and 100 μL of KBr solution (0.4 M) were subsequently injected into the solution, which was followed by the addition of gold dendritic particle solutions. The solution was shaken and then kept undisturbed for 2 h at room temperature. Then, the solution was centrifuged, and the precipitate was washed with Milli-Q water.

For the time-dependent series of CD and UV-vis spectra, the XNDs after synthesis were washed twice by centrifugation to get rid of the growth solution and prevent the alteration of the particle shapes. XNDs at 1, 3, and 5 min were not stable in dispersion due to decrease of electrostatic repulsion between the particles.

Equipment. The morphology was analyzed by scanning transmission electron microscopy (STEM) using JEOL 3100 R05, operated at 300 kV, and Thermo Fisher Talos F200X G2 S/TEM, operated at 200 kV. Electron tomography studies at room temperature were carried out on a Thermo Fisher Talos F200X G2 S/TEM equipped with a Gatan One View bottom mount camera for high-speed 4k × 4k and an X-FEG high-brightness Schottky type field emission gun (FEG) operating at 200 kV. A series of 2D projection images were recorded by tilting the specimen from −70 to 70° at nominal magnification of 150,000 using a Fischione Tomography holder Model 2020 with high tilt angles ($\chi = \pm 70^\circ$). A tomography reconstruction software package, Gatan GMS 3, was used to align the tilt series and calculate three-dimensional tomograms using a weighted back projection algorithm. CD and UV-vis spectra were obtained by a JASCO J-815.

ASSOCIATED CONTENT

SI Supporting Information

The Supporting Information is available free of charge at <https://pubs.acs.org/doi/10.1021/acsnano.4c12964>.

Additional methods, data, and comments exemplified by methodology for calculation of chirality measures, extraction of GT models, FDTD computations, and XND generation using the graph Hamiltonians ([PDF](#))

AUTHOR INFORMATION

Corresponding Author

Nicholas A. Kotov — Department of Chemical Engineering, University of Michigan, Ann Arbor, Michigan 48109, United States; Biointerfaces Institute, Center of Complex Particle Systems (COMPASS), and Department of Materials Science, University of Michigan, Ann Arbor, Michigan 48109, United States; orcid.org/0000-0002-6864-5804; Email: kotov@umich.edu

Authors

Vera Kuznetsova — Department of Chemical Engineering, University of Michigan, Ann Arbor, Michigan 48109, United States; Biointerfaces Institute, University of Michigan, Ann Arbor, Michigan 48109, United States; School of Chemistry, Trinity College Dublin, Dublin D02 PN40, Ireland

Alain Kadar — Department of Chemical Engineering, University of Michigan, Ann Arbor, Michigan 48109, United States; Biointerfaces Institute and Center of Complex Particle Systems (COMPASS), University of Michigan, Ann Arbor, Michigan 48109, United States

Anita Gaenko — Department of Chemical Engineering, University of Michigan, Ann Arbor, Michigan 48109, United States; Biointerfaces Institute and Center of Complex Particle Systems (COMPASS), University of Michigan, Ann Arbor, Michigan 48109, United States

Engin Er — Department of Chemical Engineering, University of Michigan, Ann Arbor, Michigan 48109, United States; Biointerfaces Institute and Center of Complex Particle Systems (COMPASS), University of Michigan, Ann Arbor, Michigan 48109, United States; Biotechnology Institute, Ankara University, Ankara 06135, Turkey; orcid.org/0000-0002-7713-3704

Tao Ma — Department of Materials Science, University of Michigan, Ann Arbor, Michigan 48109, United States; orcid.org/0000-0002-0579-8045

Kody G. Whisnant — Department of Chemical Engineering, University of Michigan, Ann Arbor, Michigan 48109, United States; Biointerfaces Institute and Center of Complex Particle Systems (COMPASS), University of Michigan, Ann Arbor, Michigan 48109, United States; orcid.org/0000-0003-3994-0748

Jessica Ma — Department of Chemical Engineering, University of Michigan, Ann Arbor, Michigan 48109, United States; Biointerfaces Institute and Center of Complex Particle Systems (COMPASS), University of Michigan, Ann Arbor, Michigan 48109, United States

Bing Ni — Department of Chemical Engineering, University of Michigan, Ann Arbor, Michigan 48109, United States; Biointerfaces Institute and Center of Complex Particle Systems (COMPASS), University of Michigan, Ann Arbor, Michigan 48109, United States

Natasha Mehta — Department of Chemical Engineering, University of Michigan, Ann Arbor, Michigan 48109, United States; Biointerfaces Institute and Center of Complex Particle Systems (COMPASS), University of Michigan, Ann Arbor, Michigan 48109, United States

Ji-Young Kim — Department of Chemical Engineering, University of Michigan, Ann Arbor, Michigan 48109, United States; Biointerfaces Institute, University of Michigan, Ann Arbor, Michigan 48109, United States; Present Address: Chemical and Biological Engineering, Rensselaer

Polytechnic Institute, Troy, New York 12180, United States

Yuriii K. Gun'ko — School of Chemistry, Trinity College Dublin, Dublin D02 PN40, Ireland; orcid.org/0000-0002-4772-778X

Complete contact information is available at:
<https://pubs.acs.org/10.1021/acsnano.4c12964>

Author Contributions

▀ V.K. and A.K. contributed equally.

Notes

The authors declare no competing financial interest.

ACKNOWLEDGMENTS

The authors are grateful for support from the U.S. National Science Foundation under Cooperative Agreement No. 2243104, "Center for Complex Particle Systems (COMPASS)" Science and Technology Center. The authors are grateful for the financial support from NSF Grant #2317423 Lock-and-Key Interactions of Proteins and Chiral NPs. The authors thank Anderson Toddy for his assistance with graphic design and the preparation of illustrations for this manuscript. E.E. thanks to U.S. Fulbright Visiting Scholar Program, which is sponsored by the U.S. Department of State and Turkish Fulbright Commission for post-doctoral research fellowship.

REFERENCES

- (1) Dias, A. P.; da Silva Santos, S.; da Silva, J. V.; et al. Dendrimers in the context of nanomedicine. *Int. J. Pharm.* **2020**, *573*, No. 118814.
- (2) Rao, C.; Tam, J. P. Synthesis of Peptide Dendrimer. *J. Am. Chem. Soc.* **1994**, *116*, 6975–6976.
- (3) Viltres, H.; López, Y. C.; Leyva, C.; et al. Polyamidoamine dendrimer-based materials for environmental applications: A review. *J. Mol. Liq.* **2021**, *334*, No. 116017.
- (4) Qiu, Z.-L.; Fang, L. F.; Shen, Y. J.; et al. Ionic Dendrimer Based Polyamide Membranes for Ion Separation. *ACS Nano* **2021**, *15*, 7522–7535.
- (5) Kim, A.; et al. Symmetry-breaking in patch formation on triangular gold NPs by asymmetric polymer grafting. *Nat. Commun.* **2022**, *13*, No. 6774.
- (6) Chen, Y. Shaped Hairy Polymer Nanoobjects. *Macromolecules* **2012**, *45*, 2619–2631.
- (7) Roh, S.; Williams, A. H.; Bang, R. S.; Stoyanov, S. D.; Velev, O. D. Soft dendritic microparticles with unusual adhesion and structuring properties. *Nat. Mater.* **2019**, *18*, 1315–1320.
- (8) Xia, Y.; Nguyen, T. D.; Yang, M.; et al. Self-assembly of self-limiting monodisperse supraparticles from polydisperse Nanoparticles. *Nat. Nanotechnol.* **2011**, *6*, 580.
- (9) Cao, Y.; Luo, B.; Javaid, A.; et al. Complex Materials with Stochastic Structural Patterns: Spiky Colloids with Enhanced Charge Storage Capacity. *Adv. Sci.* **2024**, *11*, No. 2305085.
- (10) Song, C. Y.; Yang, B. Y.; Chen, W. Q.; et al. Gold nanoflowers with tunable sheet-like petals: facile synthesis, SERS performances and cell imaging. *J. Mater. Chem. B* **2016**, *4*, 7112–7118.
- (11) Bahng, J. H.; Yeom, B.; Wang, Y.; et al. Anomalous dispersions of 'hedgehog' particles. *Nature* **2015**, *517*, 596–599.
- (12) Montjoy, D. G.; Bahng, J. H.; Eskafi, A.; Hou, H.; Kotov, N. A. Omnidispersible Hedgehog Particles with Multilayer Coatings for Multiplexed Biosensing. *J. Am. Chem. Soc.* **2018**, *140*, 7835–7845.
- (13) Jia, X.; Xu, W.; Ye, Z.; et al. Functionalized Graphene@Gold Nanostar/Lipid for Pancreatic Cancer Gene and Photothermal Synergistic Therapy under Photoacoustic/Photothermal Imaging Dual-Modal Guidance. *Small* **2020**, *16*, No. 2003707.
- (14) Zhou, H.; Jia, H.; Zhang, A.; et al. The interconversion between gold nanostars and gold nanodendrites controlled via temperature and

- the concentration of sodium dodecyl sulfonate. *J. Mol. Liq.* **2015**, *208*, 27–33.
- (15) Barveen, N. R.; Wang, T.-J.; Chang, Y.-H. Photochemical synthesis of Au nanostars on PMMA films by ethanol action as flexible SERS substrates for in-situ detection of antibiotics on curved surfaces. *Chem. Eng. J.* **2022**, *431*, No. 134240.
- (16) Cohen-Pope, S.; Crockett, J. R.; Wang, M.; et al. Morphology control of SERS-active 2D gold nanosnowflakes. *J. Mater. Chem. C* **2020**, *8*, 12427–12436.
- (17) O'Dwyer, C.; Navas, D.; Lavayen, V.; et al. Nano-Urchin: The Formation and Structure of High-Density Spherical Clusters of Vanadium Oxide Nanotubes. *Chem. Mater.* **2006**, *18*, 3016–3022.
- (18) Sebastian, V.; Lee, S.-K.; F Jensen, K. Engineering the synthesis of silica–gold nano-urchin particles using continuous synthesis. *Nanoscale* **2014**, *6*, 13228–13235.
- (19) Li, W.; Yang, X.; He, L.; et al. Self-Assembled DNA Nanocentipede as Multivalent Drug Carrier for Targeted Delivery. *ACS Appl. Mater. Interfaces* **2016**, *8*, 25733–25740.
- (20) Zhang, T.-K.; Yi, Z. Q.; Ye, K. Q.; et al. Controlled preparation of ordered dendritic nanoclusters at Au fractal biointerfaces. *Chem. Phys. Lett.* **2023**, *829*, No. 140750.
- (21) Wang, P.; Luo, S.; Boyle, L.; Zeng, H.; Huang, S. Controlled fractal growth of transition metal dichalcogenides. *Nanoscale* **2019**, *11*, 17065–17072.
- (22) Wąsik, P.; Seddon, A. M.; Wu, H.; Briscoe, W. H. Dendritic surface patterns from Bénard-Marangoni instabilities upon evaporation of a reactive ZnO nanofluid droplet: A fractal dimension analysis. *J. Colloid Interface Sci.* **2019**, *536*, 493–498.
- (23) Yang, C.; Cui, X.; Zhang, Z.; et al. Fractal dendrite-based electrically conductive composites for laser-scribed flexible circuits. *Nat. Commun.* **2015**, *6*, No. 8150.
- (24) de Martín, L.; Fabre, A.; Ruud van Ommen, J. The fractal scaling of fluidized NP agglomerates. *Chem. Eng. Sci.* **2014**, *112*, 79–86.
- (25) Tang, L.; Vo, T.; Fan, X.; et al. Self-Assembly Mechanism of Complex Corrugated Particles. *J. Am. Chem. Soc.* **2021**, *143*, 19655–19667.
- (26) Kogler, F.; Velev, O. D.; Hall, C. K.; Klapp, S. H. L. Generic model for tunable colloidal aggregation in multidirectional fields. *Soft Matter* **2015**, *11*, 7356–7366.
- (27) Stein, T. H. M.; Westbrook, C. D.; Nicol, J. C. Fractal geometry of aggregate snowflakes revealed by triple-wavelength radar measurements. *Geophys. Res. Lett.* **2015**, *42*, 176–183.
- (28) Ma, T. M.; VanEpps, J. S.; Solomon, M. J. Structure, Mechanics, and Instability of Fibrin Clot Infected with *Staphylococcus epidermidis*. *Biophys. J.* **2017**, *113*, 2100–2109.
- (29) Xu, C.; Lei, C.; Wang, Y.; Yu, C. Dendritic Mesoporous NPs: Structure, Synthesis and Properties. *Angew. Chem., Int. Ed.* **2022**, *61*, No. e202112752.
- (30) Huang, D.; Zhao, J.; Wang, M.; Zhu, S. Snowflake-like gold NPs as SERS substrates for the sensitive detection of organophosphorus pesticide residues. *Food Control* **2020**, *108*, No. 106835.
- (31) Das, G. M.; Managò, S.; Mangini, M.; De Luca, A. C. Biosensing Using SERS Active Gold Nanostructures. *Nanomaterials* **2021**, *11*, 2679.
- (32) Loukanov, A.; Arahangelova, V.; Emin, S.; Filipov, C. Engineering of functional nanosnowflakes from gold nanocarriers capped with amino-modified DNA oligonucleotides. *Microsc. Res. Tech.* **2023**, *86*, 1169–1176.
- (33) Li, B. L.; Luo, J. J.; Zou, H. L.; et al. Chiral nanocrystals grown from MoS₂ nanosheets enable photothermally modulated enantioselective release of antimicrobial drugs. *Nat. Commun.* **2022**, *13*, No. 7289.
- (34) Sui, R.; Charpentier, P. A.; Marriott, R. A. Metal Oxide-Related Dendritic Structures: Self-Assembly and Applications for Sensor, Catalysis, Energy Conversion and Beyond. *Nanomaterials* **2021**, *11*, 1686.
- (35) González-García, G.; Borjas-García, S. E.; Landeros-Paramo, L.; et al. Ag Nanoflowers and Nanodendrites Synthesized by a Facile Method and Their Antibacterial Activity. *J. Cluster Sci.* **2023**, *34*, 789–798.
- (36) Xu, L.; et al. Enantiomer-dependent immunological response to chiral NPs. *Nature* **2022**, *601*, 366–373.
- (37) Mao, X.; Kotov, N. Complexity, disorder, and functionality of nanoscale materials. *MRS Bull.* **2024**, *49*, 352–364.
- (38) Shaw, S.; Cademartiri, L. Nanowires and Nanostructures that Grow like Polymer Molecules. *Adv. Mater.* **2013**, *25*, 4829–4844.
- (39) Bi, C.; Wang, Z.; Zhao, H.; Liu, G. Cysteine-assisted overgrowth of gold nanorods to prepare highly branched gold nanoantennas with tunable morphological and plasmonic properties. *CrystEngComm* **2023**, *25*, 5486–5494.
- (40) Zheng, G.; Bao, Z.; Pérez-Juste, J.; et al. Tuning the Morphology and Chiroptical Properties of Discrete Gold Nanorods with Amino Acids. *Angew. Chem., Int. Ed.* **2018**, *57*, 16452–16457.
- (41) Lin, T.-H.; Lin, C.-W.; Liu, H.-H.; Sheu, J.-T.; Hung, W.-H. Potential-controlled electrodeposition of gold dendrites in the presence of cysteine. *Chem. Commun.* **2011**, *47*, 2044–2046.
- (42) Luo, J. J.; Zhang, H.; Zou, H. L.; et al. Tracking the Growth of Chiral Plasmonic Nanocrystals at Molybdenum Disulfide Heterostructural Interfaces. *Langmuir* **2023**, *39*, 3052–3061.
- (43) Lee, H.-E.; Lee, J.; Ju, M.; et al. Identifying peptide sequences that can control the assembly of gold nanostructures. *Mol. Syst. Des. Eng.* **2018**, *3*, 581–590.
- (44) Zhu, C.; et al. In-situ liquid cell transmission electron microscopy investigation on oriented attachment of gold NPs. *Nat. Commun.* **2018**, *9*, No. 421.
- (45) Rodríguez-Fernández, J.; Pérez-Juste, J.; Mulvaney, P.; Liz-Marzán, L. M. Spatially-Directed Oxidation of Gold NPs by Au(III)–CTAB Complexes. *J. Phys. Chem. B* **2005**, *109*, 14257–14261.
- (46) Kirner, F.; et al. Additive-controlled synthesis of monodisperse single crystalline gold NPs: interplay of shape and surface plasmon resonance. *J. Mater. Chem. C* **2020**, *8*, 10844–10851.
- (47) Okura, F. 3D modeling and reconstruction of plants and trees: A cross-cutting review across computer graphics, vision, and plant phenotyping. *Breed. Sci.* **2022**, *72*, 31–47.
- (48) Jiang, W.; Qu, Z.; Kumar, P.; et al. Emergence of complexity in hierarchically organized chiral particles. *Science* **2020**, *368*, 642–648.
- (49) Wang, M.; Vecchio, D.; Wang, C.; et al. Biomorphic structural batteries for robotics. *Sci. Rob.* **2020**, *S*, No. eaba1912.
- (50) Vecchio, D. A.; Mahler, S. H.; Hammig, M. D.; Kotov, N. A. Structural Analysis of Nanoscale Network Materials Using Graph Theory. *ACS Nano* **2021**, *15*, 12847–12859.
- (51) Wu, W.; Kadar, A.; Lee, S. H.; et al. Layer-by-layer assembled nanowire networks enable graph-theoretical design of multifunctional coatings. *Matter* **2025**, *8*, No. 101870, DOI: 10.1016/j.matt.2024.09.014.
- (52) Kollmer, J. E.; Daniels, K. E. Betweenness centrality as predictor for forces in granular packings. *Soft Matter* **2019**, *15*, 1793–1798.
- (53) Smart, A.; Umbanhowar, P.; Ottino, J. Effects of self-organization on transport in granular matter: A network-based approach. *Europhys. Lett.* **2007**, *79*, 24002.
- (54) Vecchio, D. A.; et al. Spanning Network Gels from NPs and Graph Theoretical Analysis of Their Structure and Properties. *Adv. Mater.* **2022**, *34*, No. 2201313.
- (55) Derkachova, A.; Kolwas, K.; Demchenko, I. Dielectric Function for Gold in Plasmonics Applications: Size Dependence of Plasmon Resonance Frequencies and Damping Rates for Nanospheres. *Plasmonics* **2016**, *11*, 941–951.
- (56) Chen, H.; Shao, L.; Li, Q.; Wang, J. Gold nanorods and their plasmonic properties. *Chem. Soc. Rev.* **2013**, *42*, 2679–2724.
- (57) Amendola, V.; Pilot, R.; Frasconi, M.; Maragò, O. M.; Iati, M. A. Surface plasmon resonance in gold NPs: a review. *J. Phys.: Condens. Matter* **2017**, *29*, No. 203002.
- (58) Ma, W.; Kuang, H.; Wang, L.; et al. Chiral plasmonics of self-assembled nanorod dimers. *Sci. Rep.* **2013**, *3*, No. 1934.

- (59) Obelleiro-Liz, M.; Martín, V. F.; Solís, D. M.; et al. Influence of Geometrical Parameters on the Optical Activity of Chiral Gold Nanorods. *Adv. Opt. Mater.* **2023**, *11*, No. 2203090.
- (60) Chen, J.; Gao, X.; Zheng, Q.; et al. Bottom-Up Synthesis of Helical Plasmonic Nanorods and Their Application in Generating Circularly Polarized Luminescence. *ACS Nano* **2021**, *15*, 15114–15122.
- (61) Merkl, P.; et al. Plasmonic Coupling in Silver NP Aggregates and Their Polymer Composite Films for Near-Infrared Photothermal Biofilm Eradication. *ACS Appl. Nano Mater.* **2021**, *4*, 5330–5339.
- (62) Steinhardt, P. J.; Nelson, D. R.; Ronchetti, M. Bond-orientational order in liquids and glasses. *Phys. Rev. B* **1983**, *28*, 784.
- (63) Joannopoulos, J. D.; Meade, R. D.; Winn, J. N. *Photonic Crystals: Molding the Flow of Light*; Princeton University Press, 1995.
- (64) Yang, R.; Bernardino, K.; Xiao, X.; et al. Graph Theoretical Description of Phase Transitions in Complex Multiscale Phases with Supramolecular Assemblies. *Adv. Sci.* **2024**, *11* (33), No. 2402464.
- (65) Berkolaiko, G.; Kuchment, P. *Introduction to Quantum Graphs*; American Mathematical Society, 2013.
- (66) Leunissen, M. E.; Christova, C. G.; Hyyninen, A. P.; et al. Ionic colloidal crystals of oppositely charged particles. *Nature* **2005**, *437*, 235–240.
- (67) Damasceno, P. F.; Engel, M.; Glotzer, S. C. Predictive Self-Assembly of Polyhedra into Complex Structures. *Science* **2012**, *337*, 453–457.
- (68) Dshemuchadse, J.; Damasceno, P. F.; Phillips, C. L.; Engel, M.; Glotzer, S. C. Moving beyond the constraints of chemistry via crystal structure discovery with isotropic multiwell pair potentials. *Proc. Natl. Acad. Sci. U.S.A.* **2021**, *118*, No. e2024034118.
- (69) Yu, Y.; Grazioli, G.; Unhelkar, M. H.; Martin, R. W.; Butts, C. T. Network Hamiltonian models reveal pathways to amyloid fibril formation. *Sci. Rep.* **2020**, *10* (10), No. 15668.
- (70) Batista, C. A. S.; Larson, R. G.; Kotov, N. A. Nonadditivity of NP interactions. *Science* **2015**, *350*, No. 1242477, DOI: 10.1126/science.1242477.
- (71) Diessner, E. M.; Freites, J. A.; Tobias, D. J.; Butts, C. T. Network Hamiltonian Models for Unstructured Protein Aggregates, with Application to γ D-Crystallin. *J. Phys. Chem. B* **2023**, *127*, 685–697.
- (72) Newman, M. E. J.; Barkema, G. T. *Monte Carlo Methods in Statistical Physics*; Clarendon Press, 2023.
- (73) Tang, Z.; Zhang, Z.; Wang, Y.; Glotzer, S. C.; Kotov, N. A. Self-Assembly of CdTe Nanocrystals into Free-Floating Sheets. *Science* **2006**, *314*, 274–278.
- (74) Park, J. I.; et al. Terminal supraparticle assemblies from similarly charged protein molecules and NPs. *Nat. Commun.* **2014**, *5*, No. 3593.
- (75) *Exponential Random Graph Models for Social Networks: Theory, Methods, and Applications*; Cambridge University Press: Cambridge, 2012.
- (76) Park, J.; Newman, M. E. J. Statistical mechanics of networks. *Phys. Rev. E* **2004**, *70*, No. 066117.
- (77) Grazioli, G.; Yu, Y.; Unhelkar, M. H.; Martin, R. W.; Butts, C. T. Network-Based Classification and Modeling of Amyloid Fibrils. *J. Phys. Chem. B* **2019**, *123*, 5452–5462.
- (78) Frenkel, D.; Smit, B. *Understanding Molecular Simulation: From Algorithms to Applications*; Elsevier: Amsterdam, The Netherlands, 2002.
- (79) Liu, J.; Luijten, E. Rejection-Free Geometric Cluster Algorithm for Complex Fluids. *Phys. Rev. Lett.* **2004**, *92*, No. 035504.
- (80) Torrie, G. M.; Valleau, J. P. Nonphysical sampling distributions in Monte Carlo free-energy estimation: Umbrella sampling. *J. Comput. Phys.* **1977**, *23*, 187–199.
- (81) Kumar, P.; Vo, T.; Cha, M.; et al. Photonically active bowtie nanoassemblies with chirality continuum. *Nature* **2023**, *615*, 418–424.
- (82) Zhang, H.; et al. Graph Theoretical Design of Biomimetic Aramid Nanofiber Nanocomposites as Insulation Coatings for Implantable Bioelectronics. *MRS Bull.* **2021**, *46*, 576–587.
- (83) McGlothin, C.; McGlothin, C.; Xiao, X.; et al. Autocatalytic Nucleation and Self-Assembly of Inorganic Nanoparticles into Complex Biosimilar Networks. *Angew. Chem., Int. Ed.* **2024**, No. e202413444.
- (84) Chen, L.; Ji, F.; Xu, Y.; et al. High-Yield Seedless Synthesis of Triangular Gold Nanoplates through Oxidative Etching. *Nano Lett.* **2014**, *14*, 7201–7206.